ACS APPLIED MATERIALS & INTERFACES

Research Article

www.acsami.org

Open Access on 07/08/2015

Synthesis of Multifunctional Magnetic NanoFlakes for Magnetic Resonance Imaging, Hyperthermia, and Targeting.

Antonio Cervadoro,[†,‡] Minjung Cho,[†] Jaehong Key,[†] Christy Cooper,[§] Cinzia Stigliano,[†] Santosh Aryal,[†] Audrius Brazdeikis,[∥] James F. Leary,[§] and Paolo Decuzzi*[,†]

[†]Houston Methodist Research Institute, 6670 Bertner Avenue, Houston, Texas 77030, United States

[‡]Politecnico di Torino, Corso Duca degli Abruzzi 24, Turin 10129, Italy

[§]Birck Nanotechnology Center, Purdue University, West Lafayette, Indiana47907, United States

[∥]University of Houston, Department of Physics and Texas Center for Superconductivity, Univesrity of Houston, 4800 Calhoun Road, Houston, Texas 77004, United States

S *Supporting Information*

ABSTRACT: Iron oxide nanoparticles (IOs) are intrinsically theranostic agents that could be used for magnetic resonance imaging (MRI) and local hyperthermia or tissue thermal ablation. Yet, effective hyperthermia and high MR contrast have not been demonstrated within the same nanoparticle configuration. Here, magnetic nanoconstructs are obtained by confining multiple, ∼ 20 nm nanocubes (NCs) within a deoxy-chitosan core. The resulting nanoconstructs—magnetic nanoflakes (MNFs)—exhibit a hydrodynamic diameter of 156 ± 3.6 nm, with a polydispersity index of ∼0.2, and are stable in PBS up to 7 days. Upon exposure to an alternating magnetic field of 512 kHz and 10 kA m^{-1}, MNFs provide a specific absorption rate (SAR) of ∼75 W g_{Fe}^{-1}, which is 4−15 times larger than that measured for conventional IOs. Moreover, the same nanoconstructs provide a remarkably high transverse relaxivity of ∼500 $(mM\ s)^{-1}$, at 1.41T. MNFs represent a first step toward the realization of nanoconstructs with superior relaxometric and ablation properties for more effective theranostics.

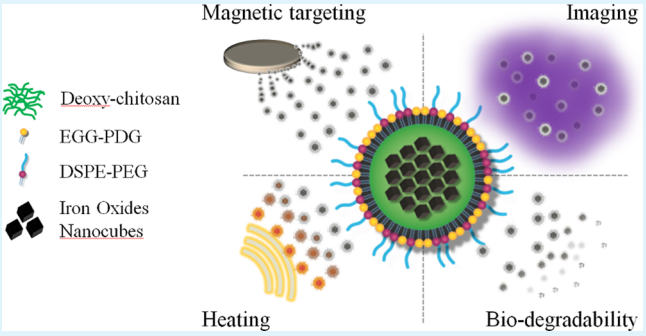

KEYWORDS: *nanoparticles, theranostic, iron oxide nanocubes, relaxivity, specific absorption rate*

INTRODUCTION

The magnetic properties of iron oxide nanoparticles (IOs) have been exploited for both imaging, diagnosis, and therapy in diverse biomedical applications.[1−5] IOs offer a significant shortening of the transverse relaxation time of water and can be efficiently used as T_2-MRI contrast agents;[6−8] also, upon exposure to alternating magnetic fields (AMF), significant amounts of heat can be deployed locally for hyperthermia and thermal ablation of the surrounding abnormal tissue.[9−11] Moreover, IOs are generally made of biodegradable iron that, upon dissolution, can enter the physiological metabolism of cells limiting possible concerns on toxicity;[12−14] and their surface can be chemically modified using a variety of well-established protocols to confer specific molecular and electrostatic properties.[15,16] Last, their intrinsic magnetic character allows for remote guidance and direct targeting via external static magnetic fields.[17,18] Therefore, the popularity of IOs derives from their intrinsic multifunctionality—imaging and therapy—which has potential applications in different biomedical fields, including oncology, cardiovascular, and neurodegenerative diseases.

A plethora of work has been dedicated to develop IOs and IO-based systems with enhanced MRI and thermal ablation performance. The effect of the size and surface properties of IOs has been systematically analyzed in numerous manuscripts showing that transverse relaxivity r_2 can be boosted by increasing the magnetic core size up to ∼30 nm,[19,20] whereas the type and thickness of polymer coatings can be detrimental to r_2 in that it could negatively affect the diffusion of water molecules and their interaction with the magnetic core.[21] For thermal ablation therapies, different heating mechanisms are involved depending on the nanoparticle size: for IOs smaller than ∼30 nm, heating is associated with Neel and Brownian relaxation; whereas hysteresis and Joule heating are the dominant effects for larger IOs. The identification of the optimal IO size range for more effective ablation therapies is still a matter for scientific debate.[22,23] Another strategy for modulating the magnetic properties of iron oxide nanoparticles has been that of forming clusters of IOs.[24−26] The mobility of the water molecules within and around the cluster is altered by the complex IO spatial organization, and the clusters can present higher transverse relaxivities as compared to the

Received: May 9, 2014
Accepted: July 8, 2014
Published: July 8, 2014

individual IO.[27,28] Recently, the shape of the IOs has been also explored as a parameter for optimizing magnetic response. Needles, star-shaped, and cubical nanoparticles have been synthesized by several groups demonstrating improved magnetic properties.[29−38]

Among the different IO shapes, iron oxide nanocubes (NCs) have demonstrated remarkable MRI and thermal ablation properties.[39] The groups of Pellegrino and Gazeau[12,29] and Hyeon and colleagues[30,31] have been synthesizing and testing NCs for their magnetic properties. The Pellegrino and Gazeau group has synthesized NCs with different sizes, ranging from ∼10 to 40 nm, and showed that small clusters of 2−3 NCs, with an edge size of ∼20 nm, would provide the highest SAR with values of ∼2500 W g_{Fe}^{-1}, at 520 kHz and 29 kA m^{-1}.[29] Comparable results have been documented by the Hyeon group using small clusters of ∼30 nm NCs.[31] In addition, the Hyeon's group has also shown that individual, ∼22 nm NCs can provide transverse relaxivities r_2 as high as 761 $(mM\ s)^{-1}$ and could be efficiently used as contrast agents in MR imaging.[30] These results would suggest that the thermal ablation behavior could mostly be achieved by using clustered NCs, whereas high contrast in MR imaging would derive by individual, ∼ 20 nm NCs.

In this work, magnetic nanoconstructs have been generated by confining multiple, individual NCs into a polymeric deoxy-chitosan matrix, which is further stabilized by an external monolayer of lipids and poly(ethylene glycol) (PEG) chains. The polymeric core is made out of deoxycholic acid-chitosan conjugate (deoxy-chitosan), and the individual NCs have an edge size of ∼20 nm and are coated with a single layer of oleic acid. The resulting nanoconstructs, called magnetic nanoflakes (MNFs), have been characterized for their physicochemical properties, stability in solution over time, relaxometric and SAR properties. A comparison of the MNFs with the original individual NCs has been also performed to demonstrate the advantages of using NC clusters to simultaneously achieve high relaxivity and SAR values.

RESULTS

Physicochemical Characterization. The magnetic nanoflakes (MNFs) were synthesized using an emulsion technique where ∼20 nm NCs, coated with a thin layer of oleic acid, are mixed with deoxy-chitosan and then covered by a lipid monolayer and poly(ethylene glycol) (PEG). A schematic representation of the MNF is shown in Figure 1a. The MNF stability and monodispersity were determined up to 7 days using standard dynamic light scattering (DLS) analysis. The data of Figure 1b show an average hydrodynamic diameter of 156 ± 3.6 nm and a polydispersity index (PDI) of ∼0.2 throughout the 7 days. The DLS data for each single day are reported in the Supporting Information, Figure S1. Transmission electron microscopy (TEM) images of the iron oxide nanocubes (NCs) used for the formation of the magnetic nanoflakes are presented in Figure 1c, where the image in the right-top inset clearly demonstrates an edge size of ∼20 nm. Electron micrographs of the whole nanoconstruct are presented in Figure 1d−f. These micrographs provide a diameter of the MNFs of ∼140 nm, under dry conditions.

As determined by inductively coupled plasma-emission spectroscopy (ICP-OES), the percentage of iron loaded into the MNFs as compared to the initial input used for synthesis (i.e., the iron yield) is 50 ± 15%. The zeta-potential of the MNFs in DI water is 37.9 ± 2.7 mV, lower than that measured

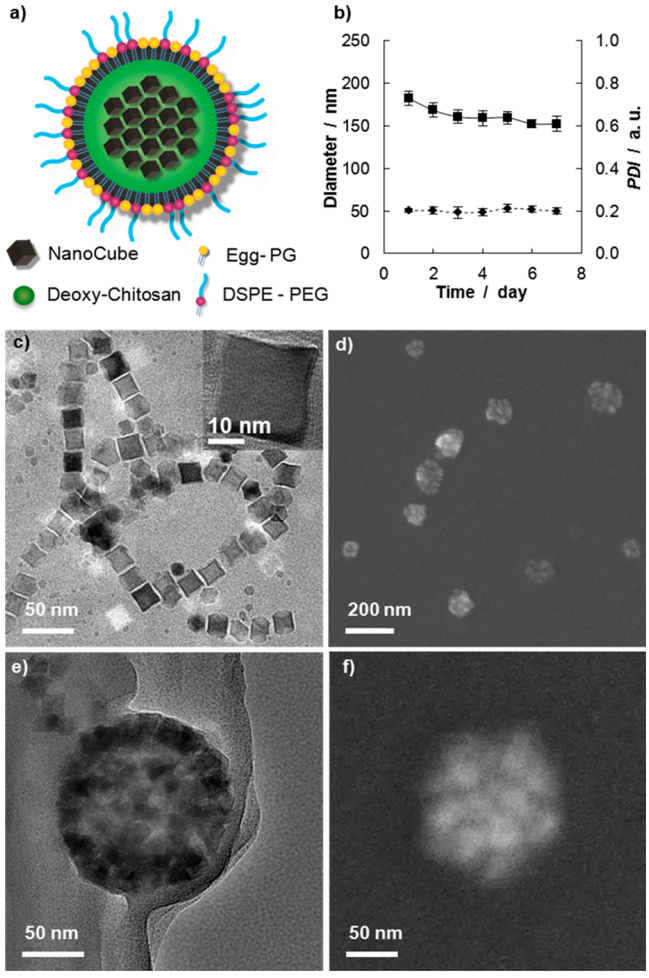

Figure 1. Physicochemical properties of the magnetic nanoflakes (MNFs): (a) Schematic representation of a MNF. (b) Stability test over time in a PBS solution (average diameter =156 ± 3.6 nm; average PDI = 0.2 ± 0.007. (c) TEM image of the nanocubes (NCs) used for the MNF synthesis. The NC edge length is ∼20 nm; (d) SEM image of the MNFs; (e, f) TEM and SEM images of the MNFs showing the NCs confined within the polymeric matrix. MNFs appear as spherical nanoconstructs with an average size of ∼140 nm.

for chitosan alone (∼46 mV). The reduction in surface electrostatic charge has to be associated with the presence of the lipid and PEG-COOH corona, which stabilizes the whole nanoconstruct. The physicochemical properties of the MNFs are summarized in Table.1.

Magnetic Characterization. The magnetic properties of the MNFs are presented in Figure 2. A magnetometer was used to characterize the magnetization M_s of the nanoconstructs as a function of the external applied field H. The magnetization curve at 300 K of Figure 2a demonstrate the lack of any hysteresis loop and a magnetization saturation of ∼80 emu g_{Fe}^{-1}, which is comparable with the values obtained by other authors. However, with a calculated magnetic susceptibility of ∼0.21, the present MNFs tend to have a lower rate of magnetization at low fields if compared with the NCs synthesized by Pellegrino and Gazeau and Hyeon.[29]

The ablation properties of the MNFs were derived by exposing the nanoconstructs to an alternating magnetic field (AMF) and registering the temperature variation of the sample over time. In particular, a vial containing an aqueous solution (0.6 mL) of MNFs (0.76 $mg_{Fe}\ mL^{-1}$) was exposed to an AMF

Table 1. Physicochemical Properties of the MNFs Compared with Other Iron Oxide Nanocubes and Nanoparticles

physical characterization		SAR (W g_{Fe}^{-1})/magnetic susceptibility		r_2 (mM^{-1} s^{-1})	
hydrodynamic size	156.9 ± 3.6 nm	magnetic nanoflakes	73.8 ± 2.3/0.21	magnetic nanoflakes	472 ± 27
core size	∼140 nm	single nanocubes	1.25 ± 0.12	WFION[48]	761
PDI	0.201 ± 0.007 a.u.	IONCs[29]	280[a]/0.4	FION[38]	324
Z-potential	37.9 ± 2.7 mV	IONCs[49]	102[a]/0.23	PVP-IO[43]	173
yielding	50 ± 15 %	Feridex[42,50]	8[a]/0.06	Feridex[38]	133

[a]Normalized to compare with our system, following the approximation SAR∝ fH^2

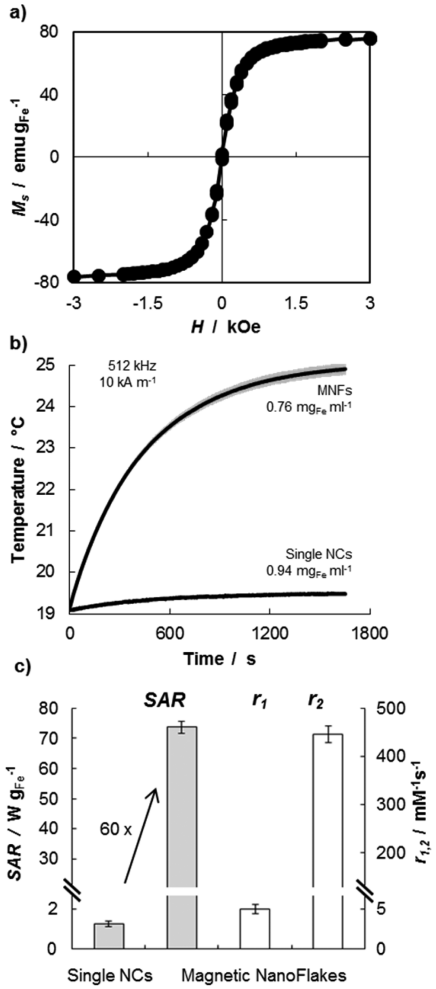

Figure 2. Magnetic properties of the magnetic nanoflakes (MNFs): (a) SQUID analysis of cycle magnetization showing the lack of any hysteresis loop and a magnetization saturation of ∼80 emu g_{Fe}^{-1}. (b) Temperature increase over time for a 0.6 mL solution of MNFs (0.76 mg_{Fe} mL^{-1}) exposed to an alternating magnetic field (512 kHz and 10 kA m^{-1} AMF) for 30 min. (c) Bar chart summarizing specific absorption rate (SAR = 73.8 ± 2.3 W g_{Fe}^{-1}) and relaxivities (r_1 = 4.98 ± 0.58 mM^{-1} s^{-1} and r_2 = 475 ± 28 mM^{-1} s^{-1}) of the MNFs. Note that the SAR of the MNFs is ∼60 times larger than that of the single NCs (1.25 ± 0.12 W g_{Fe}^{-1}).

(512 kHz, 10 kA m^{-1}) and showed an increase in temperature of ∼6 °C within 30 min (Figure 2b). The experiment was repeated 5 times returning a very small variation in temperature (gray shadow). From the temperature−time curve, the specific absorption rate of the MNFs was quantified to be 73.8 ± 2.3 W g_{Fe}^{-1}, following standard protocols. This value is ∼60 times larger than the SAR measured for the individual NCs in ethanol, which was measured to be 1.25 ± 0.12 W g_{Fe}^{-1}. This data are presented in the bar chart of Figure 2c. This significant enhancement in SAR should be attributed to the geometrical confinement of the NCs within the polymeric matrix. This geometrical confinement is responsible for modulating the diffusion of the water molecules within and around the NC clusters, which would directly affect r_2 values,[40] and for the synergistic interaction among the magnetic dipoles of adjacent clustered NCs, which would affect SAR values.[41]

The MNFs were also characterized for their ability to shorten the longitudinal and transverse relaxation time T_1 and T_2 of water. A benchtop relaxometer, operating at 1.41T and 37 °C, returned a ΔR_1 = 43.7 ± 5 (× 10^{-3} s^{-1}) and a ΔR_2 = 1.27 ± 0.13 s^{-1}, corresponding to a longitudinal relaxivity r_1 of 4.98 ± 0.58 (mM s)$^{-1}$ and a transverse relaxivity r_2 of 475 ± 28 (mM s)$^{-1}$ (Figure 2c). The iron concentration was measured to be 0.15 μg_{Fe} mL^{-1}, via ICP-OES. Note that since the individual NCs are coated with a single layer of oleic acid (i.e., are hydrophobic) and the relaxometric properties depend on the surface chemistry of the nanoparticles, the r_2 for the individual NCs could not be estimated for a direct comparison.

Finally, it should be noted that magnetic interactions are volume forces and, as such, rapidly decrease as the nanoparticle size reduces. In other words, large magnetic fields would be required to steer small IOs. However, each MNF can carry several tens of NCs which synergistically contribute to the overall magnetic dipole of the nanoconstruct. This allows us to more efficiently manipulate MNFs under flow. It is also important to emphasize that despite the large amount of iron loaded, the MNFs preserve their superparamagnetic behavior and magnetic properties over time (see the Supporting Information, Figure S2). To characterize the response to external fields, we subjected a MNF solution flowing in a parallel plate flow chamber to a static magnet field, as depicted schematically in Figure 3a. The flow rate and the chamber geometry were selected to impose a fixed, physiologically relevant wall shear rate of 100 s^{-1}. For this experiment, the MNFs were labeled with rhodamine and appeared as red dots under a fluorescent microscope. The data in panels b and c in Figure 3 clearly show that the MNFs tend to drifting laterally across the stream lines and progressively accumulate around the magnet forming a reddish corona. Indeed, in the absence of any external magnetic field, the MNFs tend to follow the flow without any lateral drift.

The surface density of the MNFs accumulating around the magnet is shown in Figure 3c and it is presented in terms of percentage of covered surface as a function of the distance y from the magnet surface. Indeed, as the separation distance from the magnet increases, the density of deposited MNFs reduces being ∼5% at ∼1.2 mm away. Note that the width of the parallel plate flow chamber is 10.0 mm, in the present configuration. The dynamics of accumulation can also be appreciated by looking at the Supporting Information, Figure S3, and, in a real time, via the Supporting Information, Movie 1,

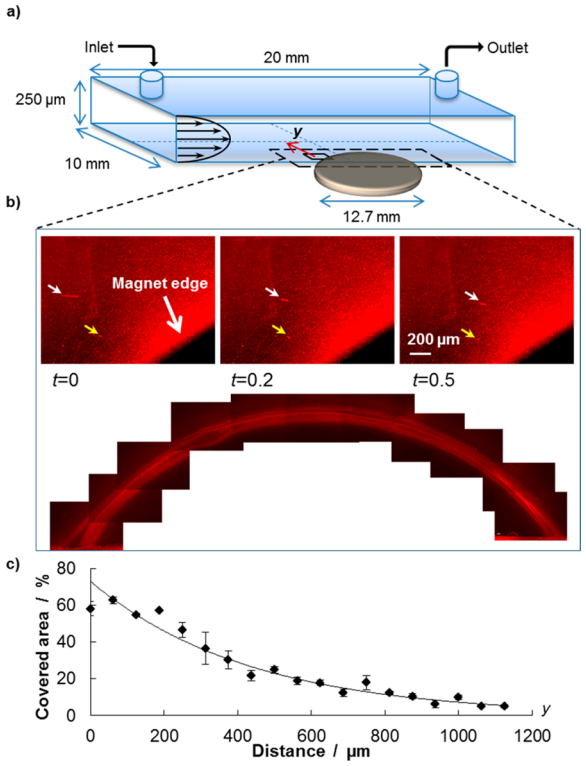

Figure 3. Remote guidance of the Magnetic NanoFlakes (MNFs): (a) Schematic representation of the parallel plate flow chamber used for the experiments. A static magnet is placed underneath the chamber for the dragging experiments under flow. (b) Three individual images show the path of two individual MNFs under flow (yellow and white arrow) at three consecutive time points; also, a fluorescent corona is formed around the magnet by the MNFs continuously depositing. The image is obtained by stitching together multiple pics taken from the unmounted coverslip after the experiment. (c) Percentage of area covered by the deposited nanoparticles is plotted as a function of the separation distance y from the magnet edge. Up to 5% of the area is covered by MNFs at ~1 mm away from the magnet.

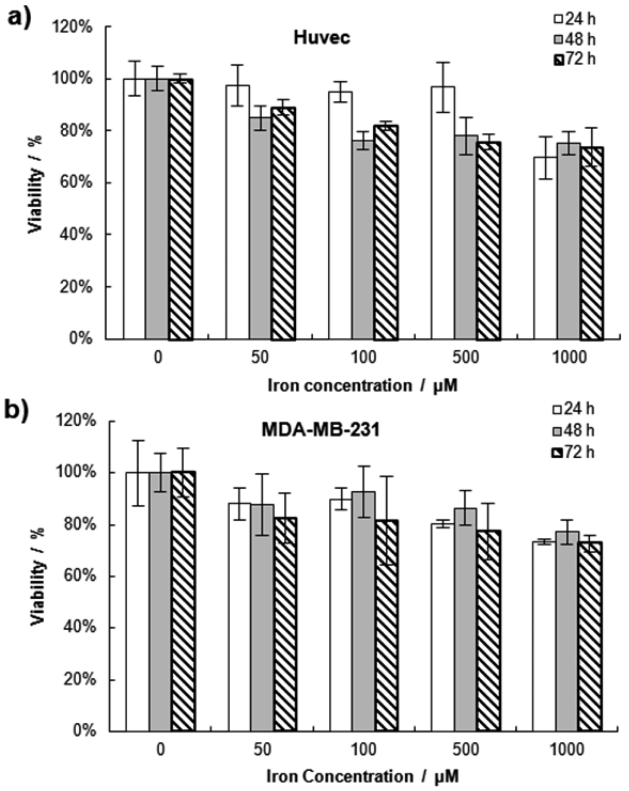

Figure 4. Cytotoxicity of the MNFs: (a) cell viability of HUVECs and (b) breast cancer MDB-MB-231. Cell viability is determined by MTT assay, at three different time points and four different MNF concentrations.

clearly demonstrating the lateral drifting of MNFs. In proximity of the magnet, the deposited MNFs cover up to 60% of the available surface.

Cytotoxicity Essay. The cytotoxic behavior of the MNFs was characterized on endothelial cells (HUVECs), which represent the first cell type encountered by nanoconstructs upon system injection, and a breast cancer cell line (MDA-MB-231). Different concentrations of MNFs were incubated with the cells and cell viability was monitored at 24, 48, and 72 h post incubation using a MTT assay. As shown in Figure 4a, during the first day of incubation, no loss in viability was observed for the HUVECs up to concentrations of 500 μM. Only at 1000 μM did the HUVEC's viability drop to 70%. Similarly, some negligible toxicity (i.e., viability <90%) was detected at concentrations larger than 100 μM for the second and third days of analysis. A similar trend was observed for the MDA-MB-231, but the toxicity was overall lower than what documented for the HUVECs. Cell viability was higher than 80% for concentrations of 500 μM up to 72h. Only at the highest concentration, of 1000 μM, did the cell viability of the MDA-MB-231 drop below 80%.

DISCUSSION

The specific absorption rate (SAR) is a dosimetric quantity that has been introduced for assessing the amount of absorbed radiation power by unit mass of tissue. It depends on the operating conditions of the AMF apparatus used for stimulating the IOs, namely the frequency f and field strength H. The data reported by Dennis and Ivkov[41] clearly show a nonlinear variation of SAR over a wide range of fH^2. However, the same data also show that this relationship can be considered as piecewise linear. In other words, within a relatively small range of fH^2, an approximate comparison of the ablation properties of different nanoparticles can be performed by normalizing the *SAR* by fH^2. This is indeed the case of the nanoparticles presented in Figure 5, where fH^2 varies between 5 and 80 × 10^{13} A^2 m^{-2} s^{-1}. Consequently, referring to the current operating conditions (f = 512 kHz and H = 10 kA m^{-1}), the SAR of ~2500 W g_{Fe}^{-1} reported by Pellegrino&Gazeau group would rescale to ~280 W g_{Fe}^{-1}. Similarly, the *SAR* values for 5 nm USPIOs[11] and the Feridex[42] nanoparticles would be equal to ~20 and ~8 W g_{Fe}^{-1}, respectively. The magnetic nanoflakes presented a SAR of 73.8 ± 2.3 W g_{Fe}^{-1}. Although the SAR of the MNFs is ~4 times lower than that measured by Pellegrino and Gazeau's group, it is still 4 −15 times larger than the SAR depicted for more conventional systems. The difference in SAR between the MNFs and the Pellegrino and Gazeau's NCs could be attributed to the different magnetic behavior of the individual NCs. In particular, the magnetic susceptibility of the Pellegrino&Gazeau's NCs is at least two times larger than that of the NCs used here, and of all other IO formulations (Figure 5a). The bar chart also confirms that SAR and magnetic

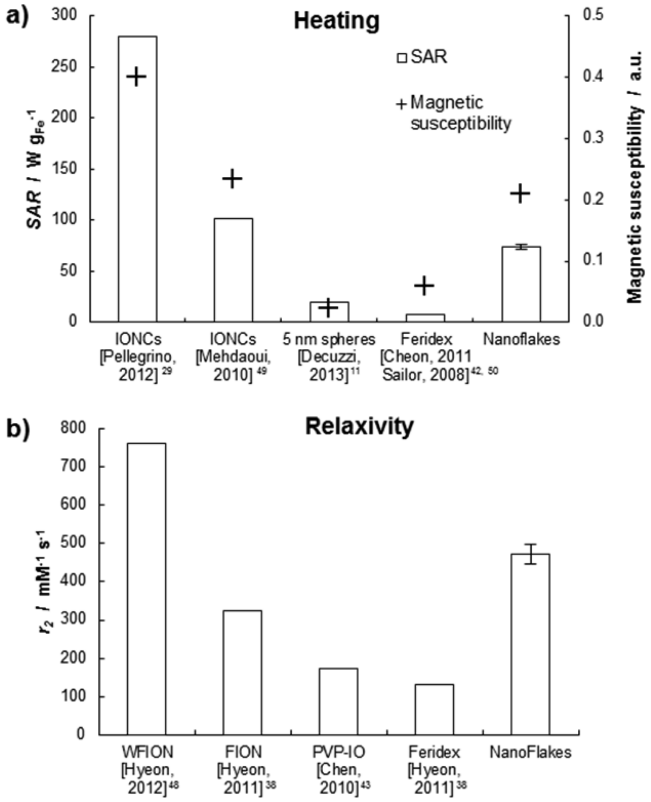

Figure 5. Performance of the MNFs: (a) Bar chart for specific absorption rate (SAR) and magnetic susceptibility. SAR values have been normalized following the approximation SAR$\propto fH^2$. Susceptibility values have been extrapolated by the cited publications. (b) Transverse relaxivity r_2.

susceptibility are directly related. Because the SAR of the MNFs is 60 times larger than that of the oleic acid-coated NC (1.25 ± 0.12 W g_{Fe}^{-1}), it is reasonable to speculate that even larger SAR could be reached for the MNFs by confining NCs exhibiting higher magnetic susceptibility.

As per the MR imaging capability, the group of Hyeon has shown that single, 22 nm NCs can provide transverse relaxivities r_2 as high as 761 $(mM\ s)^{-1}$ (Figure 5b). Importantly, this large relaxivity value has been never demonstrated for clustered NCs. The present work shows that remarkably high relaxivities can also be achieved by forming proper clusters of NCs. The MNFs showed a transverse relaxivities r_2 of 475 ± 28 $(mM\ s)^{-1}$, which is only 40% smaller than that measured by Hyeon for individual NCs. This value is significantly larger than that offered by other IOs and IO-based systems, such as the FIONs (r_2 = 324 $(mM\ s)^{-1}$),[38] PVP-IOs (r_2 = 173$(mM\ s)^{-1}$),[43] and the Feridex nanoparticle (r_2 = 133$(mM\ s)^{-1}$).[38] This transverse relaxivity is also larger than that documented for clusters generated with conventional spherical IOs. For instance, the group of Simard has demonstrated a r_2 up to 400 $(mM\ s)^{-1}$;[25] whereas the group of Morales has obtained r_2 up to ∼300 $(mM\ s)^{-1}$.[26] Moreover, the authors have recently demonstrated r_2 ∼ 500 $(mM\ s)^{-1}$ by confining conventional 5 nm IOs into discoidal polymeric matrices.[44] It is then possible that even larger relaxivities could be achieved by packing better performing individual NCs in polymer matrices.

The presented data demonstrate that magnetic nanoflakes can combine together a remarkably high relaxivity (475 ± 28 $(mM\ s)^{-1}$), specific absorption rate (73.8 ± 2.3 W g_{Fe}^{-1}, at f = 512 kHz and H = 10 kAm^{-1}), and show potentials for in vivo efficient magnetic targeting that cannot be simultaneously achieved by using either individual NCs or IO nanospheres.

CONCLUSIONS

In this study, new magnetic nanoconstructs − Magnetic NanoFlakes (MNFs) − have been derived by geometrically confining iron oxide nanocubes of ∼20 nm in edge length within a polymeric matrix of deoxy-chitosan. Following such a strategy, a remarkably high transverse relaxivity (r_2 = 475 ± 28 $(mM\ s)^{-1}$ at 1.41T) and specific absorption rate (SAR = 73.8 ± 2.3 W g_{Fe}^{-1}, at f = 512 kHz and H = 10 kAm^{-1}) have been achieved for the same nanoconstructs. It has been confirmed a significant enhancment in magnetic properties of the individual NCs upon their geometrical confinement within the polymeric matrix. In particular, the SAR of the MNFs was increased by ∼60 times over that of individual NCs (= 1.25 ± 0.12 W g_{Fe}^{-1}). The geometrical confinement of NCs exhibiting higher magnetic properties, particularly in terms of magnetic susceptibility and magnetization saturation, could lead to even higher SAR and r_2 values. These MNFs represent a first step toward the realization of nanoconstructs with superior theranostic capabilities.

EXPERIMENTAL SECTION

Nanocube Synthesis. The synthesis of the iron oxide NCs has been extensively described by Kim et al.[45] Briefly, iron(III) acetylacetonate (0.71 g), oleic acid (1.27 g), benzyl ether (10.40 g), and 4-biphenylcarbocylic (0.41 g) are mixed in a three neck flask, and then degassed by nitrogen gas (1 h) before reaction. The mixture is heated up to 290 °C and kept react for 30 min. The mixture is then cooled down and the produced nanocubes can be precipitated by ethanol. A magnetic separator of Dexter Magnetic Technologies Inc. (Elk Grove Village, IL) is employed to remove supernatant. The purified nanocubes are resuspended in chloroform. Iron(III) acetylacetonate, 4-biphenylcarboxylic acid, and benzyl ether are from Thermo Fisher Scientific Inc. (Waltham, MA). Oleic acid is obtained from Sigma-Aldrich Corp (St. Louis, MO).

Particle Synthesis. Prior to nanoconstruct synthesis, deoxycholic acid−modified chitosan conjugate (deoxy-chitosan) was synthesized following the published protocol described by Lee et al.[46] Briefly, chitosan (80 mg) was dissolved in a 9/1 (v/v) solution of DMSO/water, and then deoxycholic acid (200 mg) activated by EDC/NHS in the presence of catalytic amount TEA was added, as demonstrated in the Supporting Information, Figure S4a. The products were then purified by extensive dialysis and lyophilized to obtain dry powder. The synthesized deoxy-chitosan was characterized using FT-IR spectroscopy (see the Supporting Information, Figure S4b). The synthesis of the MNFs follows an emulsion procedure, 1% acetic acid in water (10 mL) containing 1,2-distearoyl- *sn*-glycero-3-phosphoethanolamine-*N*-[carboxy(polyethylene glycol)-2000] (750 μg) (1 mg mL^{-1} of DI water, Carboxalate-DSPE-PEG, Avanti Polar Lipids, Inc.); *L*-α-phosphatidylglycerol (500 μg of) (1 mg mL^{-1} of DI water, Egg PG, Avanti Polar Lipids, Inc.), and deoxy-chitosan (1 mg) dispersed in 1% acetic acid in water (1 mg mL^{-1}) was added. Finally, for the synthesis of the nanoconstruct of magnetite (Fe_3O_4) cubes (1.1 mg) coated with a thin layer of oleic acid dispersed in chloroform, it was emulsified in the lipid, PEG, the deoxy-chitosan mixture. Following overnight evaporation of chloroform, the particles are filtrated 4 times using Millipore centrifugal filters to clean any residual of acetic acid and unformed particles, and then rediluted in Milli-Q water or PBS as needed.

Magnetic Related Properties. A superconducting quantum interference device (SQUID) was employed to verify magnetization curve and superparamagnetic behavior (Figure 2a). The magnetization measurement was carried out with a Quantum Design SQUID magnetometer MPMS-XL. DC magnetic measurement was performed

at 300 K in 0−50 Oe field. Magnetization and hysteresis curve were collected in a field ranging from −3 to 3 T at 300 K. The sample was prepared by dropping a minimum MNFs suspensions (≥300 μL) at 3000 ppm Fe in an NMR tube. The NMR tube was sealed under vacuum and placed into a plastic straw for measurements. The magnetic susceptibility was calculated from the linear phase of the magnetization curve at lower applied fields,

Heating Performances. Heating performances have been tested on a home-built hyperthermia system. The system deploys an AMF up to a frequency of 512 kHz and field strength of 10 kA m^{-1}. It is provided with a cooling system that thermally isolates the vial from the high temperature the coil reaches when the current flows in it. After 5 min sonication, the sample (600 μL) was placed in a cylindrical probe (4 mm ID × 4 cm height); an optical probe (OptiSens Instruments) is immersed to the geometrical center of the colloidal suspension to record the temperature in the farther point from the thermal exchanges at the surface. After the sample reached equilibrium temperature, the field was switched on and temperature recorded every sec for about 20 min. Specific absorption rate (SAR) was calculated based on the well-known formula[29,47]

$$\mathrm{SAR} = \left.\frac{\Delta T}{\Delta t}\right|_{t=0} c_p \frac{1}{m_{Fe}} \quad (1)$$

where T is the temperature of the colloidal suspension; t the time; c_p indicates the heat capacity of the buffer (4186 J kg^{-1} K^{-1} for water, 957 J kg^{-1} K^{-1} for chloroform); m_{Fe} is the final mass fraction of iron in the sample. To properly calculate the first factor on the right handed term, *Mathematica 9* was used to extrapolate the close formulation for $T(t)$ in each single experiment starting from the measured temperature profile (Figure 2b).

MRI Relaxometry. To assess the relaxivity of our particles, we used a benchtop relaxometer (mq60 "The Minispec", from Bruker) with field strength of 1.41 T. For each synthesized batch, 2000 times diluted samples were prepared in Milli-Q water; dilutions were in triplicate, such to minimize approximation errors. r_1 and r_2 are calculated as

$$r_i = \left(\frac{1}{T_i} - \frac{1}{T_i^w}\right)/[\mathrm{Fe}] \quad (2)$$

In which T_i^w represents the proton relaxation time for the water, and T_i is for the sample.

In-flow dragging. Using a commercially available flow-chamber (GlicoTech) we reproduced the same shear rate the particles would be subjected during sistemic circulation. On the coverslip side of the chamber we placed a small discoidal magnet (1.6 mm H × 12.7 mm D, grade N48 - Apex Magnet, Inc.), which express a magnetic pull force of 35.6 N at 0.33 mm distance (L50 distance of the magnet against steel). The final channel sizes are 250 μm height × 10 mm widht × 20 mm length, and the magnet is placed at the channel half way, on its side (Figure 3a). In this asset, MNFs particles treated with a red fluorescent dye have been pushed in at concentration of 9 μg_{Fe} ml^{-1}, and with a shear rate of 100 s^{-1} to simulate the same conditions of tumoral vasculature. We used a fluorescence microscope to record the flow in the area around the magnet (Figure 3b, and the Supporting Information, Movie S1); the fluorescence intensity was measured using *Image-J* software, and plotted versus the distance from the magnet edge (Figure 3c). In addition, after removal of the magnet from the chamber bottom, a mosaic of images has been put together. This image demonstrate clearly the magnetic dragging and accumulation potentiality of these particles.

Cytotoxicity. Two cell lines were employed to test toxicity of our compound: (i) Human umbilical vein endothelial cells (HUVECs) obtained from PromoCell; and (ii) breast adenocarcinoma (MDA-MB-231) obtained from ATCC. Cells were originally cultured in a 10 cm Petri-dish, then seeded over a total of 6 plates (96-wells plate, ∼14 000 cells per well) to perform 3 time points per cell lines. HUVEC cell line was grown until the sixth passage in endothelial growth medium at 37 °C in a humidified 5% CO_2 atmosphere; MDA-MB-231 cancer cell line was cultured in Leibowitz L-15 medium supplemented with 10% FBS and antibiotics (100 U mL^{-1} penicillin G, 100 mg mL^{-1} streptomycin), and grown at 37 °C in a free gas exchange with atmospheric air. Cells were treated with five different iron concentrations (0, 50, 100, 500, 1000 μM) of NF-Cubes, and each concentration was in 5 replicates. MTT viability tests (3-(4,5-dimethylthiazol-2-yl)-2,5-Diphenyltetrazolium Bromide, from Invitrogen Life Sciences) have been run at 24, 48, and 72 h. Ten μL of MTT solution in PBS at 5 mg mL^{-1} were added to each well and incubated again until the inner of the cells looked totally stained in blue (≥2 h.); plates were then centrifuged at 2000 g for 5 min to deposit the salts crystals to the bottom of the wells; medium was replaced with 2-propanol (100 μL) (from Fisher Scientific, #A416−500) to suspend the crystals, shacked for 10 min (300 rpm), and then the absorption was read by spectrophotometer (Synergy H4 Hybrid Multi-Mode Microplate Reader, from BioTek Instruments, Inc.) at both 540 and 690 nm wavelength. Absorption at the second wavelength was subtracted from the first one to clear background noise. Final average and standard deviation of viability values are calculated over the five replications after blank subtraction. Control in pure medium was taken as reference at 100% for each plate.

■ ASSOCIATED CONTENT

Ⓢ Supporting Information

DLS reports for 7 days MNF stability, variation of the transverse relaxivity r_2 over 12 days time, after-flow micrograph of MNF cooperative accumulation, deoxy-chitosan reaction and FT-IR spectra, SAR vs magnetic susceptibility relationship, in-flow movie of MNF drifting toward magnet. This material is available free of charge via the Internet at http://pubs.acs.org.

■ AUTHOR INFORMATION

Corresponding Author

*E-mail: pdecuzzi@houstonmethodist.org.

Notes

The authors declare no competing financial interest.

■ ACKNOWLEDGMENTS

This work was supported by the Cancer Prevention Research Institute of Texas through Grant CPRIT RP110262. This work was also partially supported through grants from the National Institutes of Health (USA) (NIH) U54CA143837 and U54CA151668 and from the KIST-Purdue GRL (Global Research Laboratory) Collaboration ("Molecular imaging and nanomedicine for theragnosis using nanobiomaterials"). A.C. acknowledges travel support from the Scuola Interpolitecnica di Dottorato − SCUDO.

■ REFERENCES

(1) Laurent, S.; Forge, D.; Port, M.; Roch, A.; Robic, C.; Vander Elst, L.; Muller, R. N. Magnetic Iron Oxide Nanoparticles: Synthesis, Stabilization, Vectorization, Physicochemical Characterizations, And Biological Applications. *Chem. Rev.* **2008**, *108* (6), 2064−110.

(2) Gupta, A. K.; Gupta, M. Synthesis and Surface Engineering of Iron Oxide Nanoparticles for Biomedical Applications. *Biomaterials* **2005**, *26* (18), 3995−4021.

(3) Haun, J. B.; Yoon, T. J.; Lee, H.; Weissleder, R. Magnetic Nanoparticle Biosensors. *Wiley Interdiscip. Rev. Nanomed. Nanobiotechnol.* **2010**, *2* (3), 291−304.

(4) Huber, D. L. Synthesis, Properties, And Applications of Iron Nanoparticles. *Small* **2005**, *1* (5), 482−501.

(5) Corr, S. A.; Rakovich, Y. P.; Gun'ko, Y. K. Multifunctional Magnetic-Fluorescent Nanocomposites for Biomedical Applications. *Nanoscale Res. Lett.* **2008**, *3* (3), 87−104.

(6) Pittet, M. J.; Swirski, F. K.; Reynolds, F.; Josephson, L.; Weissleder, R. Labeling of Immune Cells for in Vivo Imaging Using Magnetofluorescent Nanoparticles. *Nat. Protoc.* **2006**, *1* (1), 73−79.

(7) Lanza, G. M.; Abendschein, D. R.; Yu, X.; Winter, P. M.; Karukstis, K. K.; Scott, M. J.; Fuhrhop, R. W.; Scherrer, D. E.; Wickline, S. A. Molecular Imaging and Targeted Drug Delivery with a Novel, Ligand-Directed Paramagnetic Nanoparticle Technology. *Acad. Radiol.* **2002**, *9* (Suppl 2), S330−1.
(8) Jun, Y. W.; Jang, J. T.; Cheon, J. Magnetic Nanoparticle Assisted Molecular MR Imaging. *Adv. Exp. Med. Biol.* **2007**, *620*, 85−106.
(9) Gazeau, F.; Levy, M.; Wilhelm, C. Optimizing Magnetic Nanoparticle Design for Nanothermotherapy. *Nanomedicine* **2008**, *3* (6), 831−844.
(10) Johannsen, M.; Thiesen, B.; Wust, P.; Jordan, A. Magnetic Nanoparticle Hyperthermia for Prostate Cancer. *Int. J. Hyperthermia* **2010**, *26* (8), 790−5.
(11) Cervadoro, A.; Giverso, C.; Pande, R.; Sarangi, S.; Preziosi, L.; Wosik, J.; Brazdeikis, A.; Decuzzi, P. Design Maps for the Hyperthermic Treatment of Tumors with Superparamagnetic Nanoparticles. *PLoS One* **2013**, *8* (2), e57332.
(12) Lartigue, L.; Alloyeau, D.; Kolosnjaj-Tabi, J.; Javed, Y.; Guardia, P.; Riedinger, A.; Pechoux, C.; Pellegrino, T.; Wilhelm, C.; Gazeau, F. Biodegradation of Iron Oxide Nanocubes: High-Resolution in Situ Monitoring. *ACS Nano* **2013**, *7* (5), 3939−52.
(13) Lee, C. M.; Cheong, S. J.; Kim, E. M.; Lim, S. T.; Jeong, Y. Y.; Sohn, M. H.; Jeong, H. J. Nonpolymeric Surface-Coated Iron Oxide Nanoparticles for in Vivo Molecular Imaging: Biodegradation, Biocompatibility, And Multiplatform. *J. Nucl. Med.* **2013**, *54* (11), 1974−80.
(14) Kunzmann, A.; Andersson, B.; Thurnherr, T.; Krug, H.; Scheynius, A.; Fadeel, B. Toxicology of Engineered Nanomaterials: Focus on Biocompatibility, Biodistribution, and Biodegradation. *Biochim. Biophys. Acta* **2011**, *1810* (3), 361−73.
(15) Hao, R.; Xing, R.; Xu, Z.; Hou, Y.; Gao, S.; Sun, S. Synthesis, Functionalization, And Biomedical Applications of Multifunctional Magnetic Nanoparticles. *Adv. Mater.* **2010**, *22* (25), 2729−42.
(16) Gupta, A. K.; Naregalkar, R. R.; Vaidya, V. D.; Gupta, M. Recent Advances on Surface Engineering of Magnetic Iron Oxide Nanoparticles and Their Biomedical Applications. *Nanomedicine* **2007**, *2* (1), 23−39.
(17) Dames, P.; Gleich, B.; Flemmer, A.; Hajek, K.; Seidl, N.; Wiekhorst, F.; Eberbeck, D.; Bittmann, I.; Bergemann, C.; Weyh, T. Targeted Delivery of Magnetic Aerosol Droplets to the Lung. *Nat. Nanotechnol.* **2007**, *2* (8), 495−499.
(18) Corr, S. A.; Byrne, S. J.; Tekoriute, R.; Meledandri, C. J.; Brougham, D. F.; Lynch, M.; Kerskens, C.; O'Dwyer, L.; Gun'ko, Y. K. Linear assemblies of magnetic nanoparticles as MRI contrast agents. *J. Am. Chem. Soc.* **2008**, *130* (13), 4214−4215.
(19) Jun, Y. W.; Seo, J. W.; Cheon, A. Nanoscaling Laws of Magnetic Nanoparticles and Their Applicabilities in Biomedical Sciences. *Acc. Chem. Res.* **2008**, *41* (2), 179−189.
(20) Smolensky, E. D.; Park, H. Y.; Zhou, Y.; Rolla, G. A.; Marjanska, M.; Botta, M.; Pierre, V. C. Scaling Laws at the Nano Size: The Effect of Particle Size and Shape on the Magnetism and Relaxivity of Iron Oxide Nanoparticle Contrast Agents. *J. Mater. Chem. B: Mater. Biol. Med.* **2013**, *1* (22), 2818−2828.
(21) Tong, S.; Hou, S.; Zheng, Z.; Zhou, J.; Bao, G. Coating Optimization of Superparamagnetic Iron Oxide Nanoparticles for High T2 Relaxivity. *Nano Lett.* **2010**, *10* (11), 4607−13.
(22) Fortin, J. P.; Wilhelm, C.; Servais, J.; Menager, C.; Bacri, J. C.; Gazeau, F. Size-Sorted Anionic Iron Oxide Nanomagnets As Colloidal Mediators for Magnetic Hyperthermia. *J. Am. Chem. Soc.* **2007**, *129* (9), 2628−2635.
(23) Etheridge, M. L.; Bischof, J. C. Optimizing Magnetic Nanoparticle Based Thermal Therapies Within the Physical Limits of Heating. *Ann. Biomed. Eng.* **2013**, *41* (1), 78−88.
(24) Josephson, L.; Lewis, J.; Jacobs, P.; Hahn, P. F.; Stark, D. D. The Effects of Iron Oxides on Proton Relaxivity. *Magn. Reson. Imaging* **1988**, *6* (6), 647−653.
(25) Paquet, C.; de Haan, H. W.; Leek, D. M.; Lin, H. Y.; Xiang, B.; Tian, G.; Kell, A.; Simard, B. Clusters of superparamagnetic Iron Oxide Nanoparticles Encapsulated in a Hydrogel: A Particle Architecture Generating a Synergistic Enhancement of the T2 Relaxation. *ACS Nano* **2011**, *5* (4), 3104−12.
(26) Roca, A. G.; Veintemillas-Verdaguer, S.; Port, M.; Robic, C.; Serna, C. J.; Morales, M. P. Effect of nanoparticle and Aggregate Size on the Relaxometric Properties of MR Contrast Agents Based on High Quality Magnetite Nanoparticles. *J. Phys. Chem. B* **2009**, *113* (19), 7033−9.
(27) Matsumoto, Y.; Jasanoff, A. T2 Relaxation Induced by Clusters of Superparamagnetic Nanoparticles: Monte Carlo Simulations. *Magn. Reson. Imaging* **2008**, *26* (7), 994−8.
(28) Vuong, Q. L.; Gillis, P.; Gossuin, Y. Monte Carlo Simulation and Theory of Proton NMR Transverse Relaxation Induced by Aggregation of Magnetic Particles Used As MRI Contrast Agents. *J. Magn. Reson.* **2011**, *212* (1), 139−48.
(29) Guardia, P.; Di Corato, R.; Lartigue, L.; Wilhelm, C.; Espinosa, A.; Garcia-Hernandez, M.; Gazeau, F.; Manna, L.; Pellegrino, T. Water-Soluble Iron Oxide Nanocubes with High Values of Specific Absorption Rate for Cancer Cell Hyperthermia Treatment. *ACS Nano* **2012**, *6* (4), 3080−91.
(30) Lee, N.; Choi, Y.; Lee, Y.; Park, M.; Moon, W. K.; Choi, S. H.; Hyeon, T. Water-Dispersible Ferrimagnetic Iron Oxide Nanocubes with Extremely High r(2) Relaxivity for Highly Sensitive in Vivo MRI of Tumors. *Nano Lett.* **2012**, *12* (6), 3127−31.
(31) Bae, K. H.; Park, M.; Do, M. J.; Lee, N.; Ryu, J. H.; Kim, G. W.; Kim, C.; Park, T. G.; Hyeon, T. Chitosan Oligosaccharide-Stabilized Ferrimagnetic Iron Oxide Nanocubes for Magnetically Modulated Cancer Hyperthermia. *ACS Nano* **2012**, *6* (6), 5266−73.
(32) Wang, T.; Wang, X.; LaMontagne, D.; Wang, Z.; Cao, Y. C. Shape-Controlled Synthesis of Colloidal Superparticles from Nanocubes. *J. Am. Chem. Soc.* **2012**, *134* (44), 18225−8.
(33) Buonsanti, R.; Grillo, V.; Carlino, E.; Giannini, C.; Gozzo, F.; Garcia-Hernandez, M.; Garcia, M. A.; Cingolani, R.; Cozzoli, P. D. Architectural Control of Seeded-Grown Magnetic-Semicondutor Iron Oxide-TiO2 Nanorod Heterostructures: The Role of Seeds in Topology Selection. *J. Am. Chem. Soc.* **2010**, *132* (7), 2437−2464.
(34) Palchoudhury, S.; Xu, Y.; Rushdi, A.; Holler, R. A.; Bao, Y. Controlled Synthesis of Iron Oxide Nanoplates and Nanoflowers. *Chem. Commun.* **2012**, *48* (85), 10499−501.
(35) Yoon, T. J.; Lee, H.; Shao, H.; Hilderbrand, S. A.; Weissleder, R. Multicore Assemblies Potentiate Magnetic Properties of Biomagnetic Nanoparticles. *Adv. Mater.* **2011**, *23* (41), 4793−4797.
(36) Felfoul, O.; Mokrani, N.; Mohammadi, M.; Martel, S. Effect of the chain of magnetosomes embedded in magnetotactic bacteria and their motility on magnetic resonance imaging. In *2010 Annual International Conference of the IEEE Engineering in Medicine and Biology Society*; IEEE: Piscataway, NJ, **2010**; pp 4367−4370.
(37) Liu, Y.; Chen, Q. Synthesis of magnetosome chain-like structures. *Nanotechnology* **2008**, *19* (47), 475603.
(38) Lee, N.; Kim, H.; Choi, S. H.; Park, M.; Kim, D.; Kim, H. C.; Choi, Y.; Lin, S.; Kim, B. H.; Jung, H. S.; Kim, H.; Park, K. S.; Moon, W. K.; Hyeon, T. Magnetosome-like ferrimagnetic iron oxide nanocubes for highly sensitive MRI of single cells and transplanted pancreatic islets. *Proc. Natl. Acad. Sci. U.S.A.* **2011**, *108* (7), 2662−7.
(39) Martinez-Boubeta, C.; Simeonidis, K.; Makridis, A.; Angelakeris, M.; Iglesias, O.; Guardia, P.; Cabot, A.; Yedra, L.; Estradé, S.; Peiró, F. Learning from Nature to Improve the Heat Generation of Iron-Oxide Nanoparticles for Magnetic Hyperthermia Applications. *Sci. Rep.* **2013**, *3*, No. 1652.
(40) Chiavazzo, E.; Fasano, M.; Asinari, P.; Decuzzi, P. Scaling Behaviour for the Water Transport in Nanoconfined Geometries. *Nat. Commun.* **2014**, *5*, 4565.
(41) Dennis, C. L.; Ivkov, R. Physics of Heat Generation Using Magnetic Nanoparticles for Hyperthermia. *Int. J. Hyperthermia* **2013**, *29* (8), 715−729.
(42) Lee, J. H.; Jang, J. T.; Choi, J. S.; Moon, S. H.; Noh, S. H.; Kim, J. W.; Kim, J. G.; Kim, I. S.; Park, K. I.; Cheon, J. Exchange-Coupled Magnetic Nanoparticles for Efficient Heat Induction. *Nat. Nanotechnol.* **2011**, *6* (7), 418−22.

(43) Huang, J.; Bu, L.; Xie, J.; Chen, K.; Cheng, Z.; Li, X.; Chen, X. Effects of Nanoparticle Size on Cellular Uptake and Liver MRI with Polyvinylpyrrolidone-Coated Iron Oxide Nanoparticles. *ACS Nano* **2010**, *4* (12), 7151−7160.
(44) Key, J.; Aryal, S.; Gentile, F.; Ananta, J. S.; Zhong, M.; Landis, M. D.; Decuzzi, P. Engineering Discoidal Polymeric Nanoconstructs with Enhanced Magneto-Optical Properties for Tumor Imaging. *Biomaterials* **2013**, *34* (21), 5402−10.
(45) Kim, D.; Lee, N.; Park, M.; Kim, B. H.; An, K.; Hyeon, T. Synthesis of Uniform Ferrimagnetic Magnetite Nanocubes. *J. Am. Chem. Soc.* **2009**, *131* (2), 454−5.
(46) Lee, J. Y.; Lee, S. H.; Oh, M. H.; Kim, J. S.; Park, T. G.; Nam, Y. S. Prolonged Gene Silencing by Sirna/Chitosan-G-Deoxycholic Acid Polyplexes Loaded within Biodegradable polymer nanoparticles. *J. Controlled Release* **2012**, *162* (2), 407−13.
(47) Fortin, J.-P.; Wilhelm, C.; Servais, J.; Ménager, C.; Bacri, J. C.; Gazeau, F. Size-Sorted Anionic Iron Oxide Nanomagnets as Colloidal Mediators for Magnetic Hyperthermia. *J. Am. Chem. Soc.* **2007**, *129* (9), 2628−2635.
(48) Lee, N.; Choi, Y.; Lee, Y.; Park, M.; Moon, W. K.; Choi, S. H.; Hyeon, T. Water-Dispersible Ferrimagnetic Iron Oxide Nanocubes with Extremely High R(2) Relaxivity for Highly Sensitive in Vivo MRI of Tumors. *Nano Lett.* **2012**, *12* (6), 3127−31.
(49) Mehdaoui, B.; Meffre, A.; Lacroix, L. M.; Carrey, J.; Lachaize, S.; Gougeon, M.; Respaud, M.; Chaudret, B. Large Specific Absorption Rates in the Magnetic Hyperthermia Properties of Metallic Iron Nanocubes. *J. Magn. Magn. Mater.* **2010**, *322* (19), L49−L52.
(50) Park, J. H.; von Maltzahn, G.; Zhang, L.; Schwartz, M. P.; Ruoslahti, E.; Bhatia, S. N.; Sailor, M. J. Magnetic Iron Oxide Nanoworms for Tumor Targeting and Imaging. *Adv. Mater.* **2008**, *20* (9), 1630−1635.